

Crystal structure and photoluminescence of (Gd,Ce)₄(SiS₄)₃ and (Y,Ce)₄(SiS₄)₃

Yasushi Nanai¹, Katsuhiko Suzuki², and Tsuyoshi Okuno¹

¹Department of Engineering Science, The University of Electro-Communications,
Chofu, Tokyo 182-8585, Japan

²Department of Physics, Osaka University, Toyonaka, Osaka 560-0043, Japan

E-mail: nanai-yss@tcc.pc.uec.ac.jp

Abstract. Structural and photoluminescence (PL) properties of undoped and Ce³⁺-doped rare-earth thiosilicate (Gd_{1-x}Ce_x)₄(SiS₄)₃ ($0 \leq x \leq 0.1$) and (Y_{1-x}Ce_x)₄(SiS₄)₃ ($0 \leq x \leq 0.3$) are reported. They maintain a monoclinic structure ($P2_1/n$) for the whole range of x . Increases in lattice constants appear with the increase in x because of the replacement of Gd³⁺ and Y³⁺ by larger Ce³⁺. Yellow-orange PL originating from the 5d¹-4f¹ (²F_{*J*}, $J = 5/2, 7/2$) transition of Ce³⁺ is obtained. From the measurement of PL spectra at 20 K, red shifts of the peak wavelength with the increase in x would be understood by the change of relative intensity for two luminescent centers of Ce³⁺ in PL bands. The maximum internal quantum efficiency is 62% for (Y_{0.85}Ce_{0.15})₄(SiS₄)₃. These phosphors have higher water-resistance than alkaline-earth metal thiosilicate phosphors such as Ba₂SiS₄.

1. Introduction

For the reduction of power consumption of light-emitting devices, the importance of phosphor research is increasing. Recently, thiosilicate phosphors [1, 2, 3, 4, 5, 6, 7, 8, 9] have attracted renewed attention. Thiosilicate phosphors have the advantage that low temperature is necessary for fabrication compared with silicate [10, 11, 12], silicon nitride [13, 14, 15, 16] and silicon oxynitride [17, 18, 19, 20, 21, 22, 23, 24]. This advantage is beneficial to applications for silicon photonics [25, 26, 27, 28, 29]. Visible and infrared photoluminescence of thiosilicate phosphor layer is obtained on silicon substrates. For $(Ba,Eu)Si_2S_5$, electroluminescence on silicon substrate is realized [28]. Eu^{2+} or Ce^{3+} -doped alkaline-earth metal thiosilicate phosphors have been reported as wavelength conversion materials for white light-emitting diodes [3]. However, some precautions are needed when these materials are used in practical applications because their moisture resistance is low. Compared with alkaline-earth metal thiosilicates, europium thiosilicate (Eu_2SiS_4) has high stability in moisture atmosphere. The reason might be the exclusion of alkaline-earth metals in host crystals. However, the application of Eu_2SiS_4 to phosphor materials is difficult because it has low internal quantum efficiency ($\sim 2\%$) due to concentration quenching between Eu^{2+} ions [25, 26, 29]. Rare-earth elements have similar chemical characterizations. It is expected that other rare-earth thiosilicates have high water resistance similar to Eu_2SiS_4 .

Several rare-earth thiosilicate crystals have been reported. Table 1 shows their crystal structures. $Ln_6Si_{2.5}S_{14}$ ($Ln = Y, Gd, Tb, Dy$) and $Ln_4Si_3S_{12}$ ($Ln = Ce, Pr, Nd, Sm, Gd$) were reported in 1969. After 2002, other crystal structures were reported. In table 1, only Eu_2SiS_4 was reported as host materials for phosphors [26]. There is no report of phosphor materials using rare-earth thiosilicates except Eu_2SiS_4 . Fabrication of new rare-earth thiosilicate hosts and phosphors is interesting, because of the expectation for new phosphors having high internal quantum efficiency, high moisture resistance, and applicability for silicon photonics. For the host materials of phosphor, Sc, Y, La, Gd and Lu are often used as constituent elements, because these trivalent ions have no energy transition in visible-infrared region. In this paper, $Gd_4(SiS_4)_3$ and $Y_4(SiS_4)_3$ with monoclinic structure (space group $P2_1/n$) are reported as new hosts of phosphor materials. The crystal structure and magnetic properties of monoclinic $Gd_4(SiS_4)_3$ have been reported in [34]. $Gd_4(SiS_4)_3$ and $Y_4(SiS_4)_3$ are, for the first time, demonstrated as promising host materials of phosphors in this paper. The crystal structure of $Y_4(SiS_4)_3$ is found to be the same as that of monoclinic $Gd_4(SiS_4)_3$. Fabrication of $(Gd_{1-x}Ce_x)_4(SiS_4)_3$ and $(Y_{1-x}Ce_x)_4(SiS_4)_3$ showing yellow-orange photoluminescence (PL) is reported. Broad PL spectra are obtained, and they originate from the transition from $5d^1$ excited state to $4f^1$ (2F_J , $J = 5/2, 7/2$) ground state of Ce^{3+} ions. Photoluminescence excitation (PLE) spectra having two broad bands originate from the direct excitation of Ce^{3+} ions and the indirect excitation of host materials. Efficient energy transfer from host materials to Ce^{3+} ions is realized. The maximum internal quantum efficiencies of 39% ($(Gd_{0.9}Ce_{0.1})_4(SiS_4)_3$) and 62% ($(Y_{0.85}Ce_{0.15})_4(SiS_4)_3$) are

obtained. The internal quantum efficiencies are almost preserved after the immersion in water for a day at room temperature.

2. Experimental

For the fabrication of polycrystalline $(Gd_{1-x}Ce_x)_4(SiS_4)_3$ powders, the solid-state reaction technique in a vacuum-sealed ampoule was used. A mixture of Gd_2S_3 , Ce_2S_3 , Si and S powders in the molar ratio of $2(1-x) : 2x : 3.3 : 6.6$ was prepared. The value x refers to Ce concentration in the range 0-0.1. When the value of x was 0.15, monoclinic $(Gd_{1-x}Ce_x)_4(SiS_4)_3$ was not obtained. A 10% molar excess of Si and S powder was added in the starting mixture, to remove a trace of rare-earth sulfides after thermal heating. The mixture was sealed in a silica-glass ampoule in a vacuum of 10^{-2} Pa. The ampoule was heated at 1030 °C for 24 h. When the ampoule was heated at higher temperature (1050 °C), other phases coexisted. $(Y_{1-x}Ce_x)_4(SiS_4)_3$ was fabricated in a similar fashion and x ranges between 0 and 0.3. Y_2S_3 powder was used instead of Gd_2S_3 and heating temperature was 1050 °C. When the value of x was 0.4, triclinic $Ce_6Si_4S_{17}$ phase coexisted. For investigation of water-resistance of $(Gd_{1-x}Ce_x)_4(SiS_4)_3$ and $(Y_{1-x}Ce_x)_4(SiS_4)_3$ phosphors, Eu_2SiS_4 , $(Ba_{0.99}Eu_{0.01})_2SiS_4$, $(Ba_{0.99}Eu_{0.01})Si_2S_5$ and $(Ca_{0.99}Eu_{0.01})_2SiS_4$ were fabricated and compared. Details on the fabrication of these phosphors can be found in [25, 27, 28, 29].

X-ray diffraction (XRD) patterns were recorded using a Rigaku Rint2000 diffractometer in standard θ - 2θ geometry using Cu K_α radiation. Structural information such as lattice constants was obtained using the Rietveld method[39]. The atomic positions and thermal expansion factors were not refined, as this requires higher quality XRD patterns. The measurement of PL spectra at room temperature was done using a helium-cadmium laser (325 nm, 20 mW) for the excitation. Monochromatic output of a xenon arc lamp was used for the measurement of PL spectra at 20 K and PLE spectra at 20 K and room temperature. The third harmonic of a pulsed Nd :YAG laser (355 nm, 10 Hz, pulse duration 5 ns) and a gated intensified charge-coupled device camera were used for excitation and detection in the measurement of PL decays. The time resolution was 20 ns. Internal quantum efficiency and reflectance spectra were measured using a spectrophotometer (Hamamatsu C11347-01) having an integrating sphere. Sample powder (~ 20 mg) was put on a quartz Petri dish which was placed within the integrating sphere. Monochromatic output from 300 nm to 500 nm of a xenon arc lamp was used for the excitation. Details on the measurement can be found in [28]. The water resistance of phosphors was evaluated by the measurement of its internal quantum efficiency after immersion in distilled water. Phosphor powders (20 mg) and distilled water (10 ml, 20 °C) were kept in a bottle. After 24 h, the water was removed using a dropper and then phosphor powders in the bottle were dried in an oven at 50 °C for 2 h. Except for PL and PLE spectra at 20 K, all measurements were conducted at room temperature in air atmosphere.

3. Results and discussions

3.1. XRD results

Figure 1 shows XRD patterns of (a) $(Gd_{1-x}Ce_x)_4(SiS_4)_3$ ($x = 0-0.1$) and (b) $(Y_{1-x}Ce_x)_4(SiS_4)_3$ ($x = 0-0.3$). In the top of figure 1(a) and 1(b), the simulated patterns of $Gd_4(SiS_4)_3$ and $Y_4(SiS_4)_3$ are included. $Gd_4(SiS_4)_3$ has monoclinic structure with a space group of $P2_1/n$ (no 12) [34]. For figure 1(b), it is found that the diffraction pattern of $Y_4(SiS_4)_3$ is quite similar to the monoclinic $Gd_4(SiS_4)_3$. However, $Y_4(SiS_4)_3$ having the same monoclinic structure has not been reported. Thus, the XRD pattern was calculated using the atomic positions and the thermal expansion parameters of $Gd_4(SiS_4)_3$ [34] and the lattice constants were estimated from the peak positions of the experimental pattern of $x = 0$. This simulated pattern agrees well with the experimental data ($x = 0$), and no peak of starting materials or no unidentified peak is recognized. The XRD pattern shows that the crystal structure of $Y_4(SiS_4)_3$ is the same as that of monoclinic $Gd_4(SiS_4)_3$ [34], $Tb_4(SiS_4)_3$ [35] and $Dy_4(SiS_4)_3$ [36]. This is a new crystal structure for yttrium thiosilicate which has not been reported.

From the diffraction peaks in figure 1, crystallographic data are obtained and the results are summarized in table 2. The lattice constants of $Gd_4(SiS_4)_3$ estimated in this study are in good agreement with those in [34]. The lattice constants a , b and c of $Y_4(SiS_4)_3$ is 0.6% smaller than those of $Gd_4(SiS_4)_3$. This would be reasonable because the ionic radius of Y^{3+} is 3% smaller than that of Gd^{3+} [40]. When Ce is included from the value $x=0$ to 0.1, the lattice constants a , b and c of both of the phosphors increased by 0.1%. This can be understood by the replacement of Gd^{3+} by Ce^{3+} . The ionic radius of Ce^{3+} is 9% and 12% larger than those of Gd^{3+} and Y^{3+} , respectively [40]. For $(Y_{1-x}Ce_x)_4(SiS_4)_3$, the increase of lattice constants is 0.4% from $x=0$ to 0.3. At the middle of table 2, the lattice constants of $Y_4(SiS_4)_3$ are compared with those of $Dy_4(SiS_4)_3$ [36]. The lattice constants of $Y_4(SiS_4)_3$ and $Dy_4(SiS_4)_3$ are found to be almost the same within 0.1%, because of almost the same ionic radii of Y^{3+} and Dy^{3+} [40].

3.2. Photoluminescence at room temperature

Figure 2 shows PL (right) and PLE (left) spectra of (a) $(Gd_{1-x}Ce_x)_4(SiS_4)_3$ and (b) $(Y_{1-x}Ce_x)_4(SiS_4)_3$. In all PL spectra, the single broad peak is observed. This broad PL band originates from the $5d^1-4f^1$ (2F_J , $J = 5/2, 7/2$) transition of Ce^{3+} in rare-earth sites in both of the host crystals. All PLE spectra have two excitation bands. From the measurements of reflectance spectra for $Gd_4(SiS_4)_3$ and $Y_4(SiS_4)_3$ using the integrating sphere (the spectra are not shown), the excitation bands from 300 nm to 380 nm are originated from the host absorption. The PLE spectra suggest efficient energy transfer from both of the host crystals to Ce^{3+} ions. The excitation bands from 380 nm to 500 nm are originated from the direct excitation of Ce^{3+} ions. Table 3 summaries the peak wavelength of PL and PLE spectra in figure 2(a) and 2(b). For the PLE spectrum of $(Gd_{0.99}Ce_{0.01})_4(SiS_4)_3$ ($x = 0.01$), the direct excitation peak wavelength of Ce^{3+} ions is

430 nm and shorter than that of $(Y_{0.99}Ce_{0.01})_4(SiS_4)_3$ ($x = 0.01$, 435 nm). These results are ascribed to the structural properties of $Gd_4(SiS_4)_3$ and $Y_4(SiS_4)_3$. In similar crystal structures, the crystal field splitting for 5d excited states of Ce^{3+} decreases with the increase of the distance between Ce^{3+} and adjacent ligands. The atomic coordination of $Y_4(SiS_4)_3$ has not been refined. Therefore, in this study, the coordination structure around Dy^{3+} ions in $Dy_4(SiS_4)_3$ [36] having almost the same lattice constants as $Y_4(SiS_4)_3$ is compared with that around Gd^{3+} ions in $Gd_4(SiS_4)_3$. In [34] and [36], the average distance between Gd^{3+} and S^{2-} in $Gd_4(SiS_4)_3$ is 2.911 Å, which is 0.7% larger than that between Dy^{3+} and S^{2-} in $Dy_4(SiS_4)_3$. This suggests that the lowest 5d excited state of Ce^{3+} ions in $Gd_4(SiS_4)_3$ is blue-shifted from that in $Y_4(SiS_4)_3$.

In table 3, the PL peak shifts with the increase in x (from 575 to 595 nm for $(Gd_{1-x}Ce_x)_4(SiS_4)_3$, and from 545 to 580 nm for $(Y_{1-x}Ce_x)_4(SiS_4)_3$). This red shift is not possible to be explained by the change in the lattice constants in table 2. The shift expected from table 2 would be the opposite. The red shift of the PL peak with the increase in x is possibly explained by four different Ce^{3+} sites. Monoclinic $Ln_4(SiS_4)_3$ ($Ln = Gd, Tb$ and Dy) was reported to have four sites of Ln [34]. A Ce^{3+} site dominant for PL spectra may change with the increase in x . The PL spectra in figure 2 would be composed of a few bands. This will be discussed in figure 3 using PL and PLE spectra measured at 20 K.

3.3. Photoluminescence at low temperature (20 K)

Figure 3 shows PL and PLE spectra of $(Gd_{0.99}Ce_{0.01})_4(SiS_4)_3$ and $(Y_{0.99}Ce_{0.01})_4(SiS_4)_3$ at 20 K. $(Gd_{1-x}Ce_x)_4(SiS_4)_3$ and $(Y_{1-x}Ce_x)_4(SiS_4)_3$ have similar characteristics in PL and PLE spectra. Therefore, luminescent sites were discussed using PL and PLE spectra of $(Gd_{1-x}Ce_x)_4(SiS_4)_3$ in the following paragraphs. For $(Gd_{0.99}Ce_{0.01})_4(SiS_4)_3$, two luminescent sites of Ce^{3+} can be distinguished clearly by proper choices of detection and excitation wavelength. PL spectra of figure 3(c) and 3(d) were obtained under the excitation at (c) 430 nm and (d) 470 nm, respectively. Different spectra appear for different excitation wavelength, which suggests the presence of at least two different sites for Ce^{3+} . The detection wavelength for the PLE spectrum of 3(a) was 560 nm which is the peak wavelength of the PL spectrum of figure 3(c). The detection wavelength for the PLE spectrum of figure 3(b) was 700 nm which is long-wavelength tail of the PL spectrum of figure 3(d). At 700 nm, almost no PL component is present in figure 3(c). When PLE spectra of figure 3(a) and 3(b) are compared, peak positions are different ((a) 427 nm and (b) 450 nm). The presence of two sites for Ce^{3+} is supported. In the PLE spectrum of figure 3(a), two distinct peaks can be found at 399 nm and 430 nm. These two excitation bands correspond to the transitions between the ground 4f state and the higher and lower excited 5d states of Ce^{3+} ions. The excitation peak at 450 nm in figure 3(b) corresponds to the transition between the 4f state and the lowest 5d state at a different Ce site.

To obtain the peak positions of the PL bands in figure 3(c) and 3(d), the PL

spectra were fitted using four or two Gaussian curves (not shown in the paper). Before the fitting, the horizontal axis was changed to the photon energy. Firstly, it is found that the PL spectrum of figure 3(d) is composed of two Gaussian curves having their peaks at 629 nm (1.97 eV) and 717 nm (1.73 eV). This separation (0.24 eV) is typical for the spin-orbit splitting of the $4f^1$ ground level of Ce^{3+} ions. For example, the value of the separation was 0.27 eV for $Sr_2SiS_4:Ce^{3+}$ [41]. Secondly, the PL spectrum of figure 3(c) includes two additional Gaussian peaks at 561 nm (2.21 eV) and 629 nm (1.97 eV) aside from the PL components of figure 3(d).

For $(Y_{0.99}Ce_{0.01})_4(SiS_4)_3$ of figure 3(e)-3(h), PL bands and their peaks were obtained using the same procedure as was done for $(Gd_{0.99}Ce_{0.01})_4(SiS_4)_3$. In figure 3(h), the PL spectrum is composed of two Gaussian curves with their peaks at 608 nm (2.04 eV) and 689 nm (1.80 eV). The spin-orbit splitting of the $4f^1$ ground level of Ce^{3+} in figure 3(h) is 0.24 eV. In figure 3(g), the peak positions of the two additional Gaussian curves are estimated at 546 nm (2.27 eV) and 611 nm (2.03 eV), which shows the splitting of 0.24 eV. The value of the spin-orbit splitting (0.24 eV) is the same for $(Gd_{0.99}Ce_{0.01})_4(SiS_4)_3$ and $(Y_{0.99}Ce_{0.01})_4(SiS_4)_3$. These results suggest that, in $(Gd_{0.99}Ce_{0.01})_4(SiS_4)_3$ and $(Y_{0.99}Ce_{0.01})_4(SiS_4)_3$, Ce^{3+} ions occupy the same sites having the same coordination structure.

From the measurements of PL and PLE spectra at 20 K in figure 3, two luminescent sites of Ce^{3+} are clearly observed. Gd^{3+} ions in $Gd_4(SiS_4)_3$ are reported to have 4 sites [34] which are considered to be origins of two luminescent sites. At present, it is not clear which site corresponds to the two luminescence peaks. The peak shift with the increase in the Ce concentration x shown in figure 2 and table 3 would possibly be caused by the change of the relative intensity from the two luminescence sites.

3.4. Internal quantum efficiency and relaxation process

Figure 4 shows internal quantum efficiency of $(Gd_{1-x}Ce_x)_4(SiS_4)_3$ and $(Y_{1-x}Ce_x)_4(SiS_4)_3$ when Ce^{3+} ions are excited directly and indirectly. The excitation wavelength for closed circles and diamonds was 350 nm, and the photons were absorbed by host materials (indirect excitation). Direct excitation was conducted using 435 nm (crosses) or 445 nm (open squares), and the photons were absorbed by Ce^{3+} ions. The result indicates that internal quantum efficiency is almost the same for direct and indirect excitation. This shows efficient energy transfer from the host to Ce^{3+} ions. From $x = 0.01$ to 0.1, internal quantum efficiency increases because of the increase of luminescent Ce^{3+} ions. For x values larger than 0.15 for $(Y_{1-x}Ce_x)_4(SiS_4)_3$, internal quantum efficiency does not increase anymore. Concentration quenching possibly takes place in these x values. The maximum internal quantum efficiency of $(Gd_{1-x}Ce_x)_4(SiS_4)_3$ and $(Y_{1-x}Ce_x)_4(SiS_4)_3$ are 39% ($x = 0.1$) and 62% ($x = 0.15$), respectively. The internal quantum efficiency of $(Y_{0.85}Ce_{0.15})_4(SiS_4)_3$ is close to that of some yellow phosphors. $(Y_{2.1}Gd_{0.9})Al_5O_{12}:Ce^{3+}$ yellow phosphor was reported to show the internal quantum efficiency of 72% [42]. The internal quantum efficiency 48.6% was measured in $(La,Ca)_6Si_6N_{11}:Ce^{3+}$ phosphor [43].

The present value of 62% for $(Y_{0.85}Ce_{0.15})_4(SiS_4)_3$ may be improved by fine-tuning of the synthesis condition.

To obtain decay times of $(Gd_{1-x}Ce_x)_4(SiS_4)_3$ and $(Y_{1-x}Ce_x)_4(SiS_4)_3$, time-resolved PL spectra were measured. Figure 5 shows examples for $x=0.01$. The PL intensity becomes the maximum at $t = 0$ ns when the laser pulse excites the sample. When the detection gate window delays, the intensity decreases. At 300 ns, the peak wavelengths of both the phosphors are recognized to shift from 550 nm to 610 nm for $(Gd_{0.99}Ce_{0.01})_4(SiS_4)_3$ and from 560 nm to 590 nm for $(Y_{0.99}Ce_{0.01})_4(SiS_4)_3$. These PL shifts in figure 5 suggest that each PL spectrum has two components found in figure 3. One has the short-wavelength peak with a shorter decay time, and the other has the long-wavelength peak with a longer decay time.

Figure 6 shows the decay times of the two components for $(Gd_{1-x}Ce_x)_4(SiS_4)_3$ and $(Y_{1-x}Ce_x)_4(SiS_4)_3$. To obtain the decay times of the two profiles, the integrated PL intensity in two limited ranges of wavelength was plotted against the decay time. One of the ranges is from 400 nm to 500 nm (τ_2 and τ_4 in figure 6), and the other is from 700 nm to 800 nm (τ_1 and τ_3 in figure 6). The decay time was estimated by fitting the initial decay with a single exponential function. For $(Gd_{1-x}Ce_x)_4(SiS_4)_3$, the decay times τ_1 and τ_2 decrease with the increase of the Ce concentration. The decrease of the decay time is often ascribed to the concentration quenching[27, 28]. However, the internal quantum efficiency is increased with the increase of the Ce concentration in figure 4.

In the process of spontaneous emission, decay time τ is defined as $\tau = 1/(\gamma_f + \gamma_{nr})$. γ_f and γ_{nr} represent the probability of radiative and non-radiative transitions, respectively. Herein, the decrease for τ_1 and τ_2 for $(Gd_{1-x}Ce_x)_4(SiS_4)_3$ occurs by the increase of not only the non-radiative transition but also the radiative transition. The increase of the internal quantum efficiency with the decrease of decay time is caused by the indirect excitation process from the host crystals to Ce^{3+} . For the measurement of the PL decay, the third harmonic of a pulsed Nd:YAG laser (355 nm) was used as the excitation source. Thus, it is obvious from figure 2 that Ce^{3+} ions were excited indirectly in the host crystals. The probability of energy transfer from the host crystal to Ce^{3+} ions is increased with the increase of the Ce concentration. The decay times τ_1 and τ_2 in figure 6 are considered to include the probability of energy transfer from the host to Ce^{3+} ions.

At the same value of x , $(Y_{1-x}Ce_x)_4(SiS_4)_3$ phosphors show larger efficiency than that of $(Gd_{1-x}Ce_x)_4(SiS_4)_3$ phosphors in figure 4. A possible reason would be the overlap between the energy levels of Ce^{3+} ions and the energy band of the host crystals. From the result of figure 2, the excited states of Ce^{3+} ions will probably overlap with - or close to - the conduction bands of the $Gd_4(SiS_4)_3$ and $Y_4(SiS_4)_3$ at room temperature. The PLE band of the host (300-400 nm) seems overlapped at about 400 nm with the PLE band of Ce^{3+} ions (400-500 nm) in figure 2. In that case, luminescence of Ce^{3+} ions sometimes shows quenching [44]. A host crystal whose absorption band is more overlapped with the absorption of Ce^{3+} ions is reported to have smaller PL efficiency

[44]. To estimate optical bandgaps of $Gd_4(SiS_4)_3$ and $Y_4(SiS_4)_3$ host crystals, PL and PLE spectra are obtained at 20 K, as is shown in figure 7(a). The photoluminescence of the host crystals would be ascribed to some defect states, and its internal quantum efficiency at room temperature is less than 1%. Thus PL of the host crystals does not affect the optical properties of the Ce-doped samples in this paper. PLE spectra are assumed to originate from interband transition of the host crystals. For the direct-gap semiconductor, the absorbance in the vicinity of an onset due to an electronic transition is given by

$$(\alpha h\nu)^2 \propto (h\nu - E_g), \quad (1)$$

where α is the absorption coefficient, $h\nu$ is the photon energy, and E_g is the bandgap energy. It is assumed that PL intensity is proportional to absorption coefficient. The PLE spectra may be regarded as absorption α where transmission cannot be evaluated. Figure 7(b) shows that the PLE spectra in figure 7(a) were fitted using eq.(1) (solid lines). Both spectra agree with eq.(1), and values of E_g for $Gd_4(SiS_4)_3$ and $Y_4(SiS_4)_3$ are obtained to be 3.29 eV and 3.42 eV, respectively. The energy band gap of $Gd_4(SiS_4)_3$ is narrower than that of $Y_4(SiS_4)_3$. Overlap between the absorption band of $Gd_4(SiS_4)_3$ and absorption of Ce^{3+} ions is considered to be larger than the case for $Y_4(SiS_4)_3$. Thus, the probability of the quenching for Ce^{3+} ions would be increased in $Gd_4(SiS_4)_3$ than in $Y_4(SiS_4)_3$.

To discuss the nature of transition, we calculate the first-principle band calculation for $Gd_4(SiS_4)_3$ adopting the experimentally determined lattice structure in [34]. Figure 8 (a) shows the band structure obtained using VASP package [45, 46, 47] adopting GGA-PBEsol exchange correlation functional [48]. Figure 8 (b) shows the Brillouin zone and the plotted route. The wave functions are expanded by plane waves up to cut off energy of 550 eV, and 5^3 k-mesh is used. The Fermi energy is the zero of the energy scale. In this calculation, we suppose that 4f-electrons of Gd have no contribution for the conduction band. From the result in figure 8(a), the band structure of $Gd_4(SiS_4)_3$ is clearly classified into an insulator. It is found that the bottom of the conduction band is Γ point. On the other hand, the valence band has two peaks at Γ and Z points. In figure 8(a), it is difficult to discriminate which type of direct or indirect interband transition occurs, because the energy difference between the top of the valence band at Γ and Z points is small. From the result of figure 7(b), it is suggested that the direct transition mainly occurs at Γ point in $Gd_4(SiS_4)_3$. For the estimation in figure 8(a), the band gap energy of $Gd_4(SiS_4)_3$ at Γ point is 1.74 eV. This value is about 0.5 times smaller than that of the experimental result of 3.29 eV in figure 7(b). When electric structures in solids are calculated using local-density approximation (LDA) or generalized gradient approximation (GGA) for the exchange-correlation functional, the band gap of semiconductors and insulators is severely underestimated or even absent. For example, theoretical values of fundamental band gap for GaN and ZnS using LDA were estimated to be about 0.5 times smaller compared with experimental values [49]. Thus, it is believed that the band calculation in figure 8 is reasonable as the result using

GGA-PBEsol.

3.5. Water-resistance

Table 4 shows internal quantum efficiency for thiosilicate phosphors before and after immersion in distilled water. After the immersion, the values of internal quantum efficiency for alkaline-earth metal thiosilicate phosphors were decreased below 1%. In comparison, internal quantum efficiency of $(Gd_{1-x}Ce_x)_4(SiS_4)_3$ and $(Y_{1-x}Ce_x)_4(SiS_4)_3$ have been kept over 90% of its original value. The results indicate that $(Gd_{1-x}Ce_x)_4(SiS_4)_3$ and $(Y_{1-x}Ce_x)_4(SiS_4)_3$ have higher water resistance than alkaline-earth metal thiosilicate phosphors. In [6], it was reported that the stability of alkaline-earth metal thiosilicate phosphors was significantly better than thioaluminates, and comparable to that of CaS and SrS. Thus, $(Gd_{1-x}Ce_x)_4(SiS_4)_3$ and $(Y_{1-x}Ce_x)_4(SiS_4)_3$ have distinctive advantage over these sulfide phosphors from the view point of the stability.

4. Conclusions

Novel rare-earth thiosilicate hosts $Gd_4(SiS_4)_3$ and $Y_4(SiS_4)_3$ were reported for phosphor materials. Ce^{3+} -doped $(Gd_{1-x}Ce_x)_4(SiS_4)_3$ ($0 \leq x \leq 0.1$) and $(Y_{1-x}Ce_x)_4(SiS_4)_3$ ($0 \leq x \leq 0.3$) phosphors were fabricated in powders. Monoclinic structural crystals ($P2_1/n$) were obtained. The lattice constants a , b , and c increased with x , because the ionic radius of Ce^{3+} was larger than that of Gd^{3+} and Y^{3+} . Monoclinic $Y_4(SiS_4)_3$ was a new structural phase for yttrium thiosilicate which had not been reported. Yellow-orange PL appeared and originated from the $5d^1-4f^1$ (2F_J , $J = 5/2, 7/2$) transition of Ce^{3+} ions. The PLE spectra had two bands consisting of direct excitation of Ce^{3+} and indirect excitation of host materials. The efficient energy transfer from host materials to Ce^{3+} ions was observed. At the same value of x , the PL peak wavelength of $(Gd_{1-x}Ce_x)_4(SiS_4)_3$ is longer than that of $(Y_{1-x}Ce_x)_4(SiS_4)_3$. The PL and PLE bands originating from Ce^{3+} were red-shifted with the increase in the concentration of Ce^{3+} ions. From the measurement of PL and PLE spectra at 20 K, the shifts would be caused by the change of the relative intensity for two luminescent sites of Ce^{3+} in PL bands. The maximum internal quantum efficiency was found to be 39% for $(Gd_{1-x}Ce_x)_4(SiS_4)_3$ ($x = 0.1$) or 62% for $(Y_{1-x}Ce_x)_4(SiS_4)_3$ ($x = 0.15$). In addition, these values were kept after immersion in distilled water for a day at room temperature. Compared with other thiosilicate phosphors, it was found that $(Gd_{1-x}Ce_x)_4(SiS_4)_3$ and $(Y_{1-x}Ce_x)_4(SiS_4)_3$ phosphors had the high internal quantum efficiency and high water-resistance. PLE spectra and the first-principle band calculation for $Gd_4(SiS_4)_3$ confirmed the occurrence of direct interband transition. These results are believed to be interesting for exploring new sulfide phosphor materials and applications for solid-state light sources.

Acknowledgments

XRD patterns and internal quantum efficiency were measured at Coordinated Center for UEC Research Facilities in the University of Electro-Communications. This work was supported by Grant-in-Aid for JSPS Fellows Number 13J08736.

References

- [1] Olivier-Fourcade J, Ribes M, Philippot E, Merle P, Maurin M 1975 *Mater. Res. Bull.* **10** 975-82
- [2] Smet P F, Avci N, Loos B, Van Haecke J E and Poelman D 2007 *J. Phys. Condens. Matter* **19** 246223
- [3] Smet P F, Korthout K, Van Haecke J E and Poelman D 2008 *Mater. Sci. Eng. B* **146** 264-8
- [4] Ohashi T and Ohmi K 2008 *J. Light Visual Environ.* **32** 139-42
- [5] Parmentier A B, Smet P F, Bertram F, Christen J and Poelman D 2010 *J. Phys. D: Appl. Phys.* **43** 085401
- [6] Smet P F, Moreels I, Hens Z and Poelman D 2010 *Materials* **3** 2834-83
- [7] Parmentier A B, Smet P F and Poelman D 2010 *Optical Materials* **33** 141-4
- [8] Lee S P, Huang C H, Chan T S, Chen T M 2014 *ACS Appl. Mater. Interfaces* **6** 7260-7
- [9] Lee S P, Huang C H, Chen T M 2014 *J. Mater. Chem. C* **2** 8925-31
- [10] Park J K, Lim M A, Kim C H, Park H D and Park J T 2003 *Appl. Phys. Lett.* **82** 683
- [11] Shimomura Y, Honma T, Shigeiwa M, Akai T, Okamoto K and Kijima N 2007 *J. Electrochem. Soc.* **154** J35
- [12] Zhang X and Liu X 1992 *J. Electrochem. Soc.* **139** 622
- [13] Höpfe H A, Lutz H, Morys P, Schnik W and Seilmeier A 2000 *J. Phys. Chem. Solids* **61** 2001
- [14] Li Y Q, Fang C M, de With G and Hintzen H T 2004 *J. Solid State Chem.* **177** 4687
- [15] Uheda K, Takizawa H, Endo T, Yamame H, Shimada M, Wanf C M and Mitomo M 2000 *J. Lumin.* **867** 87
- [16] Uheda K, Hirosaki N, Yamamoto Y, Naito A, Nakajima T and Yamamoto H 2006 *Electrochem Solid-State Lett.* **9** H22
- [17] Takahashi K, Hirosaki N, Kimura N, Ohashi M, Xie R-J, Harada M, Yoshimura K and Tomomura Y 2007 *Appl. Phys. Lett.* **91** 091923
- [18] Li Y Q, Delsing C A, de With G and Hintzen H T 2005 *Chem. mater.* **17** 3242
- [19] van Krevel J W N, van Rutten J W T, Mandal H, Hintzen H and Metselaar R 2002 *J. Solid State Chem.* **19** 165
- [20] Xie R-J, Mitomo M, Uheda K, Xu F F and Akimune Y 2002 *J. Am. Ceram. Soc.* **85** 1229
- [21] Xie R-J, Hirosaki N, Mitomo M, Yamamoto Y, Suehiro T and Sakuma K 2004 *J. Phys. Chem. B* **108** 12027
- [22] Xie R-J, Hirosaki N, Sakuma K, Yamamoto Y and Mitomo M 2004 *Appl. Phys. Lett.* **84** 5404
- [23] Hirosaki N, Xie R-J, Kimoto K, Sekiguchi T, Yamamoto Y, Suehiro T and Mitomo M 2005 *Appl. Phys. Lett.* **86** 211905
- [24] Xie R-J, Hirosaki N, Yamamoto Y, Suehiro T, Mitomo M and Sakuma K 2005 *Jpn. J. Ceram. Soc.* **113** 462
- [25] Nishimura M, Nanai Y, Bohda T and Okuno T 2009 *Jpn. J. Appl. Phys.* **48** 072301
- [26] Sugiyama M, Nanai Y, Okada Y and Okuno T 2011 *J. Phys. D: Appl. Phys.* **44** 095404
- [27] Nanai Y, Sasaki C, Sakamoto Y, Okuno T 2011 *J. Phys. D: Appl. Phys.* **44** 405402
- [28] Nanai Y, Sakamoto Y, Okuno T, 2012 *J. Phys. D: Appl. Phys.* **45** 265102
- [29] Nanai Y, Sakamoto Y, Okuno T 2013 *Jpn. J. Appl. Phys.* **52** 04CG15
- [30] Daszkiewicz M, Gulay L D, Ruda I R, Marchuk O V and Pietraszko A 2007 *Acta Cryst.* **E63** i197
- [31] Gauthier G, Jovic S, Evain M, Koo H-J, Whangbo M-H and Fouassier C 2003 *R. Brec, Chem. Mater.* **15** 828
- [32] Perez G and Duale M 1969 *C.R. Acad. Sci. Ser. C* **269** 984
- [33] Michelet A, Flahaut J 1969 *C.R. Acad. Sci. Ser. C* **268** 326
- [34] Hatscher S T and Umland W 2003 *J. Solid State Chem.* **172** 417
- [35] Hatscher S T and Umland W 2002 *Z. Anorg. Allg. Chem.* **628** 1673
- [36] Hatscher S T and Umland W 2002 *Acta Cryst.* **E58** i74
- [37] Gulay L D, Daszkiewicz M, Lychmanyuk O S and Pietraszko A 2008 *J. Alloys and Compounds*

453 197

- [38] Hartenbach I and Schleid T 2002 *Z. Anorg. Allg. Chem.* **628** 1327
- [39] Izumi F and Momma K 2007 *Solid State Phenom.* **130** 15
- [40] Shannon R D 1976 *Acta Cryst.* **A32** 751
- [41] Parmentier A B, Smet P F and Poelman D 2013 *Materials* **6** 3663 I
- [42] Kasuya R, Tetsuhiko Isobe T, Kuma H and Katano J 2005 *J. Phys. Chem. B* **109** 22126
- [43] Suehiro T, Hirosaki N and Xie R-J 2011 *ACS Appl. Mater. Interfaces* **3** 811
- [44] Ueda J, Tanabe S and Nakanishi T 2011 *J. App. Phys.* **110** 053102
- [45] Kresse G and J. Hafner J 1993 *Phys. Rev. B* **47** 558
- [46] Kresse G and Furthmüller 1996 *Phys. Rev. B* **54** 11169
- [47] Kresse G and Joubert D 1999 *Phys. Rev. B* **59** 1758
- [48] Perdew J P, Ruzsinszky A, Csonka G I, Vydrov O A, Scuseria G E, Constantin L A, Zhou X and Burke K 2008 *Phys. Rev. Lett.* **100** 136406
- [49] Tran F and Blaha Peter 2009 *Phys. Rev. Lett.* **102** 226401

Figure 1. XRD patterns of (a) $(Gd_{1-x}Ce_x)_4(SiS_4)_3$ and (b) $(Y_{1-x}Ce_x)_4(SiS_4)_3$. The value of x is shown in the figures. In the top of (a) and (b), the simulated patterns of $Gd_4(SiS_4)_3$ and $Y_4(SiS_4)_3$ are shown, respectively.

Figure 2. PL (right) and PLE (left) spectra of $(Gd_{1-x}Ce_x)_4(SiS_4)_3$ and $(Y_{1-x}Ce_x)_4(SiS_4)_3$. The detection wavelength for the PLE spectra is the peak of the corresponding PL spectrum. All spectra are normalized by their peak intensity.

Figure 3. PL (right) and PLE (left) spectra of $(Gd_{0.99}Ce_{0.01})_4(SiS_4)_3$ and $(Y_{0.99}Ce_{0.01})_4(SiS_4)_3$ at 20 K. For $(Gd_{0.99}Ce_{0.01})_4(SiS_4)_3$, PLE spectra are obtained for the emission at (a) 560 nm (circle) and (b) 700 nm (cross). The excitation wavelength of PL spectra is (c) 430 nm (circle) or (d) 470 nm (cross). For $(Y_{0.99}Ce_{0.01})_4(SiS_4)_3$, PLE spectra are obtained for the emission at (e) 550 nm (circle) and (f) 700 nm (cross). The excitation wavelength of PL spectra is (g) 430 nm (circle) or (h) 470 nm (cross).

Figure 4. Internal quantum efficiency of $(Gd_{1-x}Ce_x)_4(SiS_4)_3$ and $(Y_{1-x}Ce_x)_4(SiS_4)_3$. The excitation wavelength is shown in the figure.

Figure 5. Time-resolved PL spectra of $(Gd_{0.99}Ce_{0.01})_4(SiS_4)_3$ and $(Y_{0.99}Ce_{0.01})_4(SiS_4)_3$. The delay time is 0 ns (solid lines) and 300 ns (dashed lines), and the detection gate width is 10 ns. The time origin 0 ns corresponds to the time when laser excites the sample and the PL intensity is the maximum. The intensity of each spectrum is normalized by its maximum.

Figure 6. Decay times plotted against x in $(Gd_{1-x}Ce_x)_4(SiS_4)_3$ (τ_1 , τ_2) and $(Y_{1-x}Ce_x)_4(SiS_4)_3$ (τ_3 , τ_4). They were estimated from the temporal decay curves. τ_1 (closed circle) and τ_3 (open circle) were estimated by the decay curves of the PL intensity in the wavelength region between 700 nm and 800 nm. τ_2 (closed square) and τ_4 (open square) were measured for the wavelength region of 400-500 nm.

Figure 7. (a) PL and PLE spectra of $Gd_4(SiS_4)_3$ and $Y_4(SiS_4)_3$ at 20 K. The detection wavelength for the PLE spectra is the peak of the corresponding PL spectrum. The excitation wavelength for the PL spectra is 365 nm for $Gd_4(SiS_4)_3$ and 350 nm for $Y_4(SiS_4)_3$. All spectra are normalized by their peak intensity. (b) The estimation of optical band gap energies for $Gd_4(SiS_4)_3$ and $Y_4(SiS_4)_3$ using the PLE intensity which is assumed to be proportional to absorption coefficient α . Experimental data (open squares and circles) are fitted by eq. (1) (solid lines).

Figure 8. (a) Calculated energy band structure of $Gd_4(SiS_4)_3$. (b) The Brillouin zone of $Gd_4(SiS_4)_3$.

Table 1. Rare-earth thiosilicates. The composition ratio of the pseudobinary system between rare-earth sulfide (Ln_2S_3) and silicon disulfide (SiS_2) is shown. Ln is constituent elements of the crystal structure.

Composition	$Ln_2S_3 : SiS_2$	Crystal system	Space group	Ln	Reference
Ln_2SiS_5	1 : 1	Monoclinic	$P2_1/c$	La, Ce	[30, 31]
$Ln_6Si_{2.5}S_{14}$	3 : 2.5	Hexagonal	$P63$	Y, Gd, Tb, Dy	[32]
$Ln_4Si_3S_{12}$	2 : 3	Trigonal	$R3c$	Ce, Pr, Nd, Sm, Gd	[31, 33]
$Ln_4(SiS_4)_3$	2 : 3	Monoclinic	$P2_1/n$	Gd, Tb, Dy	[34, 35, 36]
$Ln_6Si_4S_{17}$	3 : 4	Triclinic	$C-1$	Ce, Pr, Nd, Sm	[31, 37]
Composition	$EuS : SiS_2$	Crystal system	Space group	Ln	Reference
Eu_2SiS_4	2 : 1	Monoclinic	$P2_1/c$	-	[38]
$EuSi_2S_5$	1 : 2	Monoclinic	$C2$	-	[28]

Table 2. Crystallographic data obtained by XRD peaks of $(Gd_{1-x}Ce_x)_4(SiS_4)_3$ and $(Y_{1-x}Ce_x)_4(SiS_4)_3$ powders with various composition.

$(Gd_{1-x}Ce_x)_4(SiS_4)_3$	a (Å)	b (Å)	c (Å)	β (degree)	Reference
$Gd_4(SiS_4)_3$	9.87	11.00	16.46	102.67	[34]
$x = 0$	9.88	11.01	16.47	102.68	
0.01	9.88	11.01	16.48	102.68	
0.05	9.88	11.01	16.48	102.68	
0.1	9.89	11.02	16.5	102.68	
$(Y_{1-x}Ce_x)_4(SiS_4)_3$	a (Å)	b (Å)	c (Å)	β (degree)	Reference
$Dy_4(SiS_4)_3$	9.81	10.94	16.36	102.86	[36]
$x = 0$	9.81	10.95	16.37	102.83	
0.01	9.81	10.94	16.37	102.83	
0.05	9.82	10.95	16.38	102.83	
0.1	9.82	10.95	16.39	102.81	
0.15	9.83	10.96	16.4	102.82	
0.2	9.84	10.97	16.42	102.82	
0.3	9.85	10.99	16.45	102.80	

Table 3. Peak wavelength of PL and PLE spectra for $(Gd_{1-x}Ce_x)_4(SiS_4)_3$ and $(Y_{1-x}Ce_x)_4(SiS_4)_3$.

$(Gd_{1-x}Ce_x)_4(SiS_4)_3$	PLE peak (nm)	PL peak (nm)
$x = 0.01$	365, 430	575
0.05	365, 430	575
0.1	365, 435	595
$(Y_{1-x}Ce_x)_4(SiS_4)_3$	PLE peak (nm)	PL peak (nm)
$x = 0.01$	360, 435	545
0.05	360, 435	560
0.1	360, 440	570
0.15	360, 440	575
0.2	360, 445	580
0.3	360, 445	580

Table 4. The internal quantum efficiency for thiosilicate phosphors before (Φ_0) and after (Φ) immersion in distilled water.

Phosphors	Φ_0	Φ
$(Gd_{0.99}Ce_{0.01})_4(SiS_4)_3$	0.20	0.20
$(Gd_{0.9}Ce_{0.1})_4(SiS_4)_3$	0.39	0.42
$(Y_{0.99}Ce_{0.01})_4(SiS_4)_3$	0.32	0.29
$(Y_{0.85}Ce_{0.15})_4(SiS_4)_3$	0.62	0.61
Eu_2SiS_4	0.02	0.02
$(Ca_{0.99}Eu_{0.01})_2SiS_4$	0.51	0.007
$(Ba_{0.99}Eu_{0.01})_2SiS_4$	0.42	0.008
$(Ba_{0.99}Eu_{0.01})Si_2S_5$	0.52	0.003

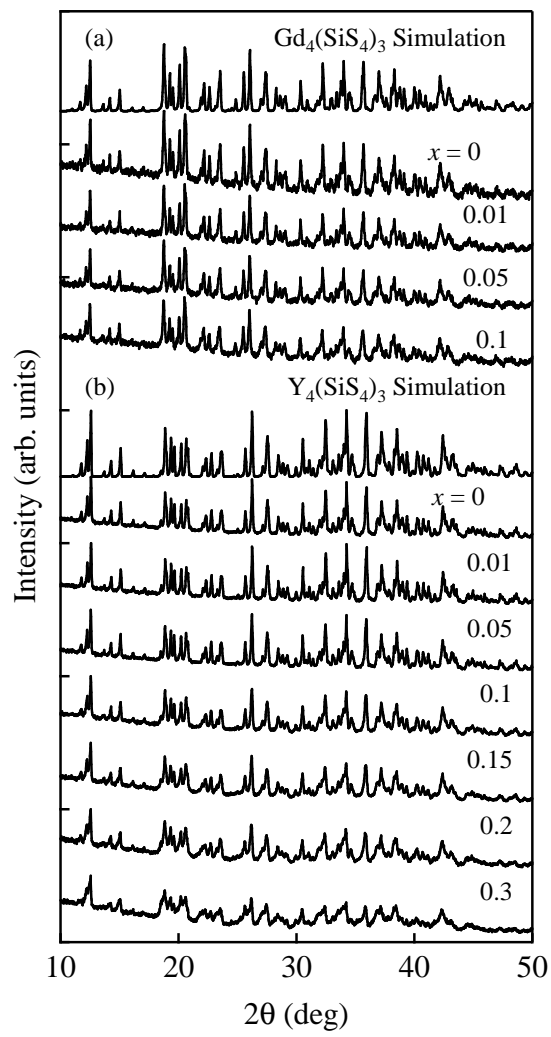


Figure 1.

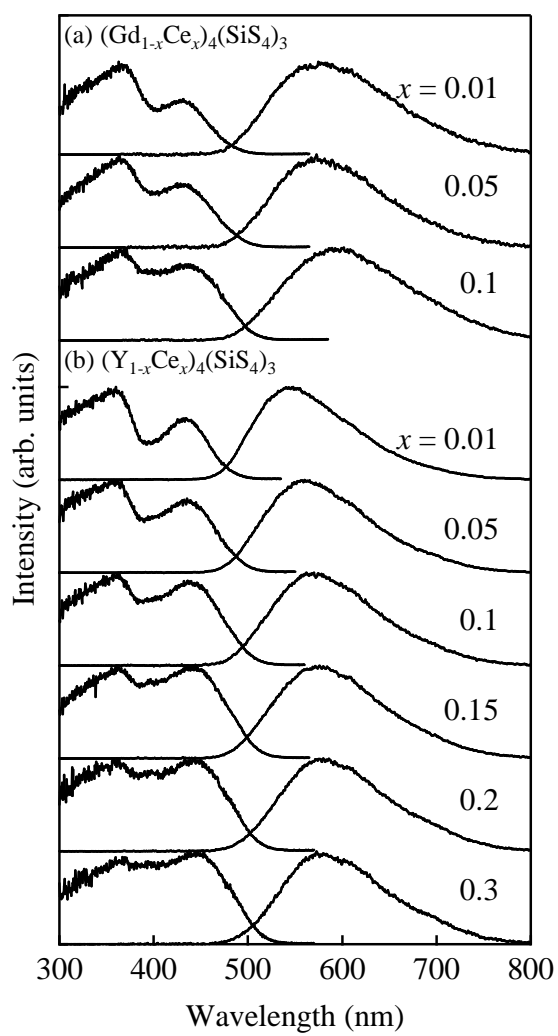


Figure 2.

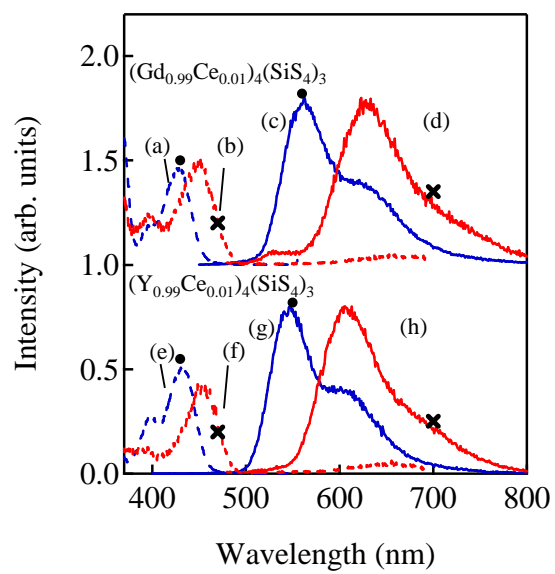


Figure 3.

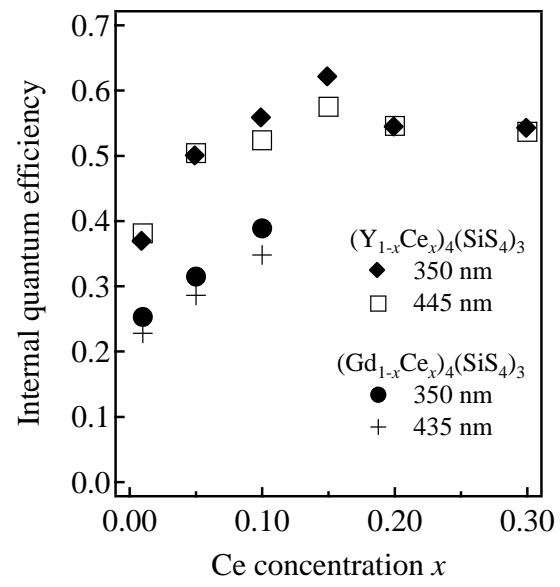


Figure 4.

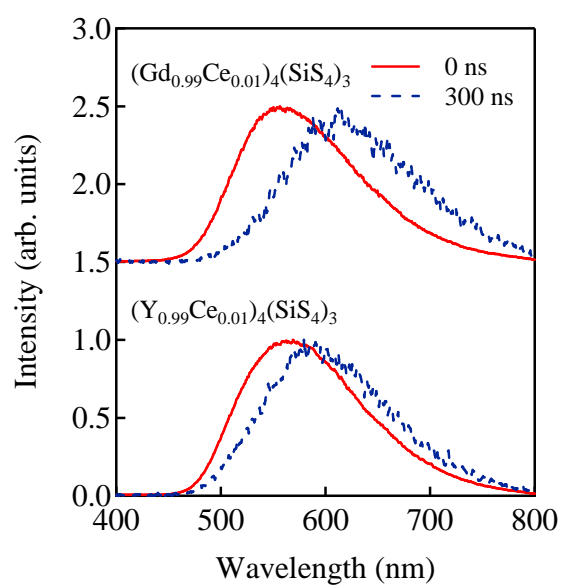


Figure 5.

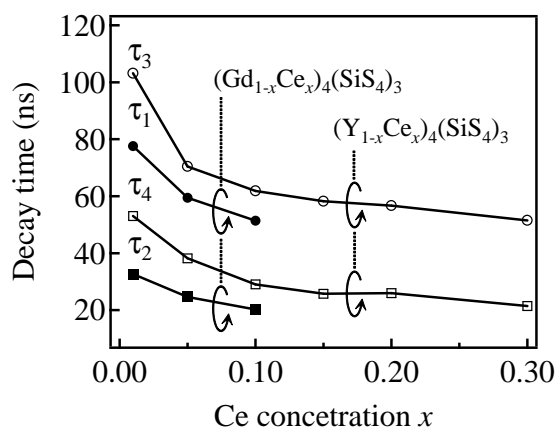


Figure 6.

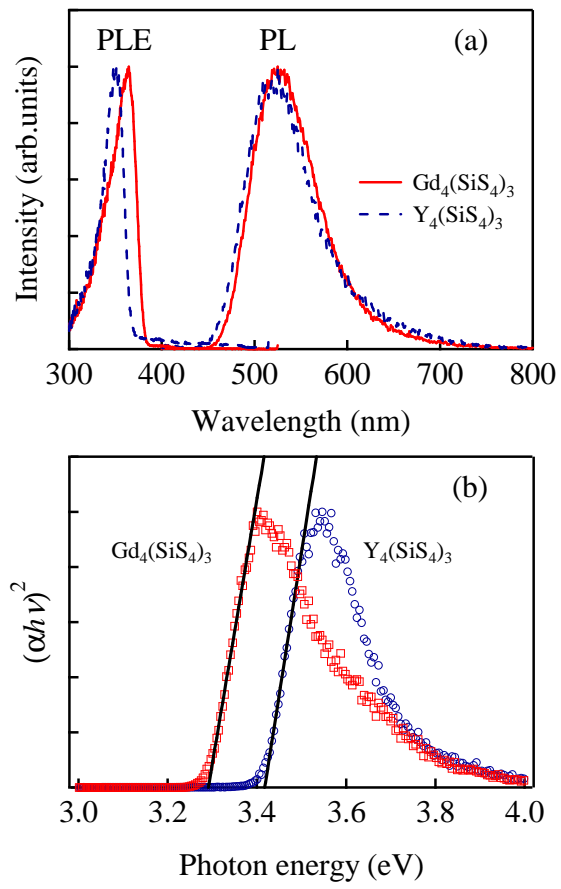


Figure 7.

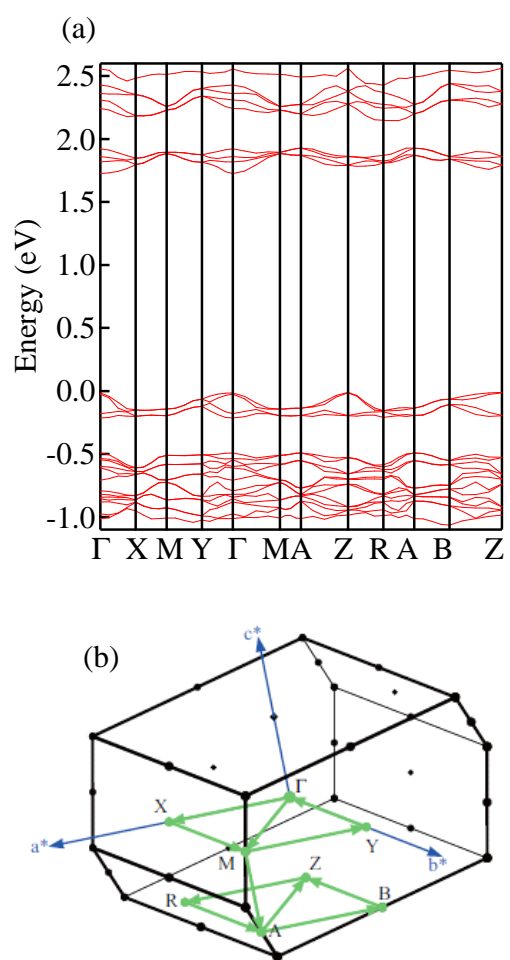


Figure 8.